research papers

An intensity evaluation method: *EVAL*-14

Albert J. M. Duisenberg,* Loes M. J. Kroon-Batenburg and Antoine M. M. Schreurs

Department of Crystal and Structure Chemistry, Bijvoet Centre for Biomolecular Research, Utrecht University, Padualaan 8, NL-3584 CH Utrecht, The Netherlands. Correspondence e-mail: a.j.m.duisenberg@chem.uu.nl

Dedicated to the memory of Jan Kroon, deceased 3 May 2001.

A reflection intensity integration method is presented based upon *ab initio* calculation of three-dimensional (x, y, ω) reflection boundaries from a few physical crystal and instrument parameters. It is especially useful in challenging circumstances, such as the case of a crystal that is far from spherical, anisotropic mosaicity, $\alpha_1\alpha_2$ peak splitting, interference from close neighbours, twin lattices or satellite reflections, and the case of streaks from modulated structures, all of which may frustrate the customary profile-learning and -fitting procedures. The method, called *EVAL*-14, has been implemented and extensively tested on a Bruker Nonius KappaCCD diffractometer.

1. Introduction

On an area-detector diffractometer, a detector image is obtained by rotating the sample crystal uniformly over a scan angle $\Delta\omega$ on a spindle by preference perpendicular to the primary X-ray beam, Fig. 1. The usually flat and stationary detector collects the reflected and scattered radiation and generates an array of pixels with numerical values representing the intensity received per pixel during the scan. Typical values for a charge-coupled device (CCD) image[1] are 620×576 pixels of 0.11×0.11 mm on a detector surface of about 6.8×6.3 cm placed at a distance of 40 mm behind the crystal, showing reflection spots of roughly 1 mm^2 (Fig. 2). The set of images holding the crude reflection data is processed to form reflection 'shoe boxes': one or more ($N_{\Delta\omega}$) consecutive $\Delta\omega$ layers of $N_x \times N_y$ pixels, with a reflection inside like a 'mouse in the bread'.

Methods to obtain net reflection intensities from detector data are known as 'evaluation methods'; see for example the work of Pflugrath & Messerschmidt (1993), who introduced the concept of shoe boxes and implemented several evaluation methods for the FAST diffractometer. We can distinguish roughly two approaches: data counting and data interpreting.

The classic *BPB* method is the most familiar example of a counting method. The net intensity $I_{net} = P - kB$, with k the ratio of the sizes of the P (peak) and the B (background) region. If only Poissonian noise is involved, and if we have a constant background or, with a linearly sloping background, a centred reflection, then $\sigma^2(I_{net}) = P + k^2B$. The values for P and B are obtained by simply counting the intensity in the respective regions, without any data manipulation whatsoever. All we need is the correct P enclosure at the right position. The position follows from the pre-established reciprocal cell and orientation matrix [**R**] [equation (1) in §2]; the shape or size is quite a different matter. For the one-dimensional case

(a classic three- or four-circle diffractometer reflection) Lehmann & Larsen (1979) recommend those P limits that maximize $I_{net}/\sigma(I)$. This, however, gives a somewhat too narrow P region (as can be demonstrated by calculations on model reflections) and the method is difficult to apply in two or three dimensions, where a reflection region is not defined solely by one simple ω range. Nevertheless, it is still useful for long-tailed peaks with hard-to-define limits, as occur often in neutron diffraction. Bolotovsky *et al.* (1995) present an original 'seed-skewness' procedure for the two-dimensional case, *i.e.* for ω-integrated reflections or reflections falling completely within one $\Delta\omega$ image. They start with a small prospective P region within the $N_x \times N_y$ data area (the seed) and let it grow pixelwise until the skewness of the distribution of the remaining data, the background, is minimal. We feel this might fail on very weak backgrounds (a rare phenomenon, admittedly), when the Poisson distribution is far from normal. Graafsma *et al.* (1997) compared this P integration method, *HIPPO*, experimentally with the well known profile fitting
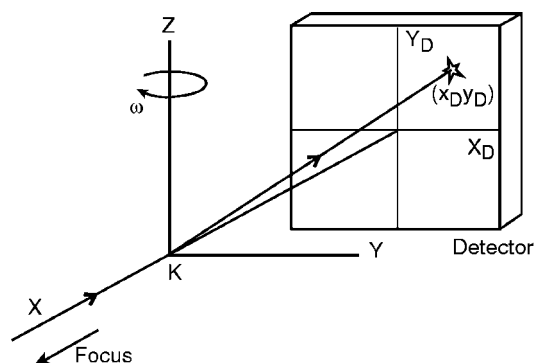
Figure 1
Schematic representation of the diffraction experiment. The sample crystal K is situated at the origin of the Cartesian laboratory system XYZ. X points to the focus centre; the $+Z$ axis runs along the rotation axis, which is perpendicular to the primary beam. One reflection is shown, with detector coordinates x_D, y_D.

program *DENZO* (Otwinowski, 1993) and found only minor differences, such as *DENZO* giving final difference maps of slightly better apparent quality, or somewhat lower R_{merge} values for *HIPPO*.
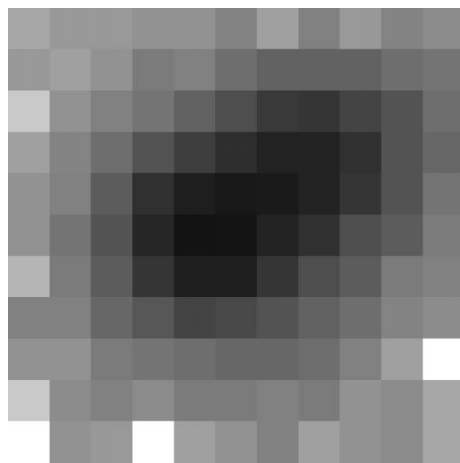
Interpretation methods typically try to scale the observed reflection profile [mostly an $I(x, y)$ histogram from ω integration] to a standard profile learnt from suitable sample reflections. The effects of statistical outliers in the profile are reduced because the individual pixel data are not accepted blindly, like in the *BPB* method, but are compared with the expected reflection shape. Most profile fitting techniques rest upon procedures developed by Diamond (1969) and Ford (1974). Rossmann (1979) and Leslie (1991) exploit various detector regions to learn local standard profiles. Kabsch (1988) improved profile learning and evaluation by redistributing the observed pixel data over an appropriate local three-dimensional grid, such that it looks like the reflection had traversed the Ewald sphere perpendicularly and had been recorded in layers locally parallel to the sphere's surface. The transformed reflections show less variation in spot size and ω width, by which fewer standard profiles are required, typically nine. Otwinowski & Minor (1997) obtain a learnt standard profile from sufficiently strong reflections within a given detector area and apply this to the weaker reflections in the same region. Bourgeois *et al.* (1998) propose a profile fitting method for the integration of weak and/or spatially overlapping reflections by applying the supposedly similar shape of suitable reflections in the immediate neighbourhood. They emphasize the importance of an optimal profile-fitting area, which we fully endorse for the *BPB* integration area or volume as well.

Profile fitting is the pre-eminent method conceptually, especially for weak reflections and for unstatistical noise (*e.g.* spikes, dead pixels) if the correct standard profile is applied at the exact reflection position; at the same time, this is its weak point. With crystals that are far from spherical, or in cases of anisotropic mosaicity, multiple lattices, satellite reflections

from modulated structures, and double-peaked reflections from α_1–α_2, it may be difficult to obtain reliable standards, if indeed they exist at all. The effects upon the profile of crystal shape, absorption or anisotropic mosaicity may result in each reflection being a standard for itself only, and then we are, in fact, left with the *BPB* method. The point is that an empirical profile learning process does not look explicitly for the physical factors that really explain the various reflection shapes: the reflection profiles are observed, manipulated, idealized and averaged, but not understood.

Alexander & Smith (1962) *predicted* the one-dimensional reflection profile for a classic equatorial single-reflection diffractometer by convoluting the 'sub-profiles' from the source size, wavelength range, and crystal shape and mosaicity (details follow in §3.1). Working on this, Keulen (1969) formulated the practical rules for the best ω-scan angle, detector aperture dimensions and especially for an optimal crystal/detector ($\omega/2\theta$) angular velocity scan ratio. Mathieson & Stevenson (1996) applied a kind of ray tracing to simulate reflection profiles for this type of diffractometer for small single-crystal spheres, not for realistic crystals. Here too optimal values for scan angle, $\omega/2\theta$ angular velocity ratio and detector aperture size for *BPB* application are obtained, albeit in quite an elaborate way. Their method is not readily applicable to three-dimensional reflection integration; it does, however, elucidate the anatomy of the Bragg reflection very well.

Though the *BPB* method has its drawbacks, we apply it in *EVAL*-14 because in many circumstances where profile learning and fitting are hindered *EVAL*-14 manages the job: it predicts the three-dimensional reflection position and boundary for each reflection (and for interfering neighbours) from a few physical instrument and crystal parameters. We feel that the *BPB* method with the correct boundary is preferable to profile fitting with an unreliable standard profile.
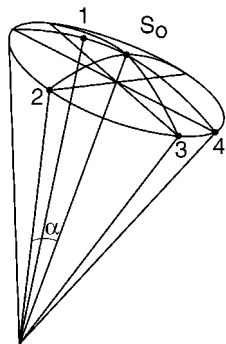
2. Elementary diffraction geometry

2.1. The central impact

We suppose a standard area diffractometer experiment as described above (Fig. 1), with crystal rotation on an axis perpendicular to the primary beam. We define an orthonormal laboratory axes system XYZ with the Z axis along the rotation axis, the X axis pointing from the crystal centre (XYZ origin) to the source centre and with the Y axis completing the right-handed Cartesian system. Angles and rotations are defined corkscrew-wise, *e.g.* $+X$ rotated over $+90°$ about $+Z$ ends on $+Y$. The $+X$ axis is the angular zero point.

The zero position of the crystal and all its direct and reciprocal vectors is that with the spindle set at $\omega = 0$.[2] Then the XYZ components of the reciprocal cell vectors **a***, **b*** and **c*** define the reciprocal-axes matrix [**R**]:

Figure 2
A reflection spot on the KappaCCD detector. The real size of this picture is about 1.2×1.2 mm with 11×11 pixels of 0.11×0.11 mm. An arbitrary grey scale is applied here.

[2] On some instruments the spindle is called φ.

$$[\mathbf{R}] = \begin{pmatrix} a_x^* & b_x^* & c_x^* \\ a_y^* & b_y^* & c_y^* \\ a_z^* & b_z^* & c_z^* \end{pmatrix}. \tag{1}$$

The reflection normal $\mathbf{S}_0(h, k, l)$ for a reflection hkl, defined in reciprocal space as $(h\mathbf{a}^* + k\mathbf{b}^* + l\mathbf{c}^*)$, has XYZ coordinates:

$$\begin{pmatrix} S_{0,x} \\ S_{0,y} \\ S_{0,z} \end{pmatrix} = [\mathbf{R}] \cdot \begin{pmatrix} h \\ k \\ l \end{pmatrix}. \tag{2}$$

The Bragg angle θ_λ for wavelength λ is given by

$$\sin\theta_\lambda = \lambda|\mathbf{S}_0|/2. \tag{3}$$

$\mathbf{S}_0$ is the reflection normal in zero position, where hkl will not reflect unless by sheer coincidence. If $\mathbf{S}_0$ can be rotated to a position $\mathbf{S}_\omega$ where it makes an angle of $90° - \theta_\lambda$ with the $+X$ axis, then and only then will hkl reflect (Fig. 3). We formulate the central reflection condition for $\mathbf{S}_\omega$ as

$$\cos\zeta = \sin\theta_\lambda / \cos\chi, \tag{4}$$

with ζ the angle between the XY projection of $\mathbf{S}_\omega$ and the X axis, and χ the elevation of $\mathbf{S}_\omega$, defined by $\sin\chi = S_{\omega,z}/|\mathbf{S}_\omega|$, which equals $S_{0,z}/|\mathbf{S}_0|$. If $\cos\zeta < 1$ then a reflecting position $\mathbf{S}_\omega$ exists for $+\zeta$, and another one for $-\zeta$. We will explain the case $\zeta > 0$ in detail; the case $\zeta < 0$ is similar.

$\mathbf{S}_0$ is brought from its original position ω_0 to the reflecting position $+\zeta$ by a spindle rotation ω:

$$\omega = \zeta - \omega_0. \tag{5}$$

Figure 3
Reflection condition for the central impact. The angle between the reflecting $\mathbf{S}_\omega$ and $+X$ must equal $90° - \theta$. Therefore $\mathbf{S}_0$, the reflection normal in zero position, must be rotated to $\mathbf{S}_\omega$ over an angle $\omega = \zeta - \omega_0$, with $\cos\zeta = \sin\theta/\cos\chi$ [equation (4)]. Note that ω is negative in this figure.

The XYZ coordinates of the reflecting $\mathbf{S}_\omega$ are:

$$\begin{aligned} S_{\omega,x} &= |\mathbf{S}_0|\cos\chi\cos\zeta, \\ S_{\omega,y} &= |\mathbf{S}_0|\cos\chi\sin\zeta, \\ S_{\omega,z} &= |\mathbf{S}_0|\sin\chi. \end{aligned} \tag{6}$$

The reflected ray departs from $(0, 0, 0)$ along $\mathbf{r}$:

$$\mathbf{r} = \mathbf{S}_\omega - \mathbf{X}/\lambda, \tag{7}$$

with $\mathbf{X}$ the unit vector along the $+X$ axis. Note that $r_x < 0$ for forward reflection, which is applied normally in area-detector diffractometry.

We obtain the central impact on the detector by lengthening $\mathbf{r}$ until it touches the detector surface. On the KappaCCD (for example) the crystal–detector distance can be set; in addition, the 'swing angle' σ between the detector normal $\mathbf{D}$ and the $-X$ axis can be set, by pivoting the detector on the Z axis; the detector horizon remains horizontal. $\mathbf{D}$ in the laboratory system XYZ is then

$$\mathbf{D} = \begin{pmatrix} -D\cos\sigma \\ -D\sin\sigma \\ 0 \end{pmatrix}, \tag{8}$$

with D the distance from the crystal to the detector. (For a detector perpendicular to the through beam, $\sigma = 0$.)

The impact $\mathbf{R}$ on this type of detector in the laboratory system XYZ is

$$\mathbf{R} = (\mathbf{D} \cdot \mathbf{D}/\mathbf{D} \cdot \mathbf{r})\mathbf{r}. \tag{9}$$

Conventionally, the detector $+X_D$ axis points to the right and the $+Y_D$ axis points upwards, seen from the crystal; therefore we define the detector system $X_D Y_D Z_D$ as follows. If $\sigma = 0$ (as in Fig. 1) X_D runs along Y, Y_D runs along Z, and Z_D along X; the system $X_D Y_D Z_D$ rotates on Z with σ. The detector centre is always at $(0, 0, -D)$ in that system, irrespective of σ. The conversion from impact $\mathbf{R}(x, y, z)$ to impact (x_D, y_D) in detector coordinates is given by

$$x_D = R_y\cos\sigma - R_x\sin\sigma, \quad y_D = R_z. \tag{10}$$

z_D is not very interesting: it always equals $-D$. Now the central impact coordinates (x_D, y_D, ω) for reflection $\mathbf{S}_0(h, k, l)$ are given by x_D and y_D from equations (10) and by ω from (5).

2.2. The general impact

For the central impact we assumed a point focus, one wavelength λ, an infinitely small crystal and one reflection vector $\mathbf{S}_0$, i.e. no mosaicity. For a general impact we take into account the source size, wavelength range, crystal shape and crystal mosaicity. We represent these factors by corresponding vector sets defined in the laboratory system XYZ, as follows.

Source: vectors ($\mathbf{F}$) to all points of the real or effective X-ray source.

Wavelengths: the one-dimensional vectors, i.e. numbers, (λ) from λ_{min} to λ_{max}.

Crystal: vectors ($\mathbf{K}$) to all points within and on the crystal in zero position. Mis-centring is automatically included if ($\mathbf{K}$) is obtained from in situ observations.
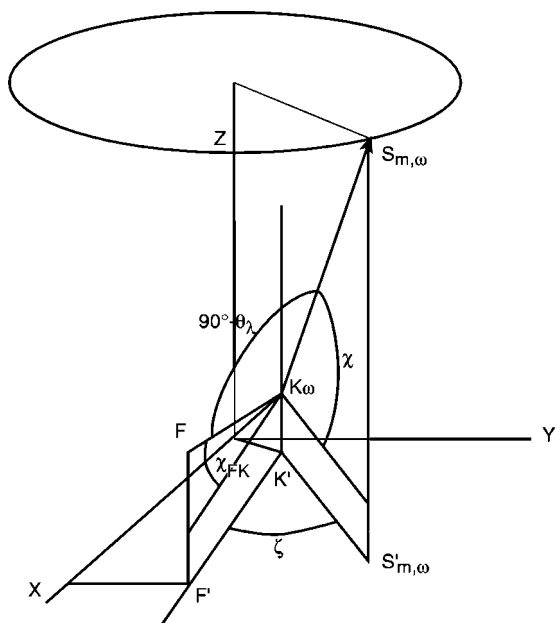
Figure 4
Mosaicity model. S_0 is the central reflection vector $S_0(h,k,l)$. With isotropic mosaicity the mosaic vectors S_m ($|S_m| = |S_0|$) form a massive circular cone around S_0, with $2\alpha = \mu$, the full mosaicity. **1** represents a general S_m vector; **2**, **3** and **4** are special ('extreme') $S_{m,E}$ vectors on the cone mantle. With anisotropic mosaicity the circular domain through (**2**, **3**, **4**) is elliptically stretched.

Isotropic mosaicity: a massive cone-shaped bundle of vectors (S_m) around the central S_0, all with length $|S_0|$ (Fig. 4). The cone angle $2\alpha = \mu$, the full isotropic mosaic spread.

Anisotropic mosaicity is described by an extra mosaicity μ_A about an anisotropy vector A, fixed in the crystal system (Duisenberg, 1983). The circular isotropic mosaic (S_m) area around S_0 (the spherically bent cone base) is elliptically stretched, preserving $|S_m| = |S_0|$, by an amount $\mu_A\sin\angle(A, S_0)$ along the direction of $A \times S_0$.

Figure 5
General reflection condition. K_ω is an arbitrary element of the crystal with an arbitrary mosaic orientation $S_{m,\omega}$ (i.e. $S_{m,\omega}$ is an arbitrary vector from the massive mosaic cone, Fig. 4). F is an arbitrary point on the focus (FK_ω runs along the incident ray $K_\omega - F$; F is not drawn). Reflection occurs only if the angle between FK_ω and $S_{m,\omega}$ equals $90° - \theta_\lambda$, with $\sin\theta_\lambda = \lambda|S_{m,\omega}|/2$. Then $\cos\zeta = (\sin\theta_\lambda - \sin\chi_{FK}\sin\chi)/(\cos\chi_{FK}\cos\chi)$ [equation (11)], with χ_{FK} the inclination of FK_ω.

The vector sets (F), (λ) and (S_m) may follow non-uniform distributions from a non-uniformly emitting source, the λ spectrum and the distribution (e.g. Gaussian) of the S_m vectors. However, this, and crystal absorption effects, do not influence the reflection boundary (which has our primary interest), but only the intensity distribution within the reflection body, the profile.

A general impact now originates from an arbitrary (F, λ, K, S_m) combination, i.e. an F to some point of the source, a number λ within the wavelength range (λ_{min}, λ_{max}), a vector K to some point within or on the crystal in zero position and, finally, a vector S_m from the massive cone of S_m vectors around S_0. The reflection condition for an (F, λ, K, S_m) selection is that the angle between K–F (the incident ray) and S_m equals $90° - \theta_\lambda$, with θ_λ following from $\sin\theta_\lambda = \lambda|S_0|/2$. In general, this condition is not met with the crystal in zero position and then S_m must be rotated over a specific angle ω to a reflecting position $S_{m,\omega}$ (by which K is rotated automatically to K_ω), such that the angle ζ between the XY projections of $S_{m,\omega}$ and $F - K_\omega$ satisfies the general reflection condition (Fig. 5):

$$\cos\zeta = (\sin\theta_\lambda - \sin\chi_{FK}\sin\chi)/(\cos\chi_{FK}\cos\chi). \quad (11)$$

In this formula χ_{FK} is the elevation of $F - K_\omega$, defined by $\sin\chi_{FK} = (F_z - K_{\omega,z})/|F - K_\omega|$, and χ the elevation of $S_{m,\omega}$, given by $\sin\chi = S_{m,z}/|S_m|$. ($S_{m,\omega}$ and S_m have the same length and elevation.) The angle ζ in (11) is not the same as that in the central impact formula, equation (4). There $\zeta = 0$ coincides with the $+X$ axis; here $\zeta = 0$ coincides with the line $F'K'_\omega$, the XY projection of the incident ray $K_\omega - F$, Fig. 6. The difference, $\delta\omega$, is given by

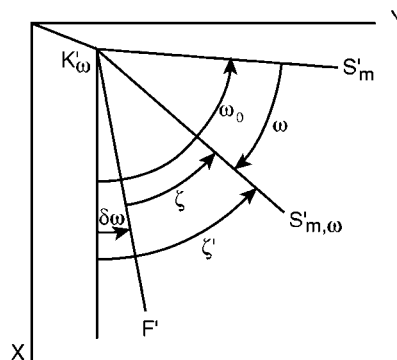$$\sin\delta\omega = (F_y - K_{\omega,y})/F'K'_\omega, \quad (12)$$

with $F'K'_\omega = |F - K_\omega|\cos\chi_{FK}$. Now the angle ζ' between the XY projection of the reflecting $S_{m,\omega}$ and the X axis is

$$\zeta' = \zeta + \delta\omega \quad (13)$$

and, finally, the rotation ω that brings S_m from its original position ω_0 to this reflecting position ζ' is

$$\omega = \zeta + \delta\omega - \omega_0. \quad (14)$$

Figure 6
Projection of Fig. 5 along Z. S'_m is the projection of $S_{m,0}$ (not shown in Fig. 5). The rotation that brings S'_m to the reflecting position $S'_{m,\omega}$ is $\omega = \delta\omega + \zeta - \omega_0$, with $\sin\delta\omega = (F_y - K_{\omega,y})/F'K'_\omega$.

To calculate ζ from (11) we need χ_{FK}, the elevation of $\mathbf{F} - \mathbf{K}_\omega$ with $\mathbf{K}_\omega$ in the final position determined by the unknown ζ itself. We solve this by repeated application of equations (11)–(14). A good starting value for ω is that for the central impact, equation (4), because then $\mathbf{K}_\omega$ cannot be more than about half the angular reflection width away from reflecting. Usually one or two iterations suffice, which is not surprising: the elevation χ_{FK} of $\mathbf{F} - \mathbf{K}_\omega$ [needed in equation (11)] with $|\mathbf{F}|$ typically $\sim$220 mm and $|\mathbf{K}| < 0.5$ mm will not change very much by rotating $\mathbf{K}$ on the Z axis.

The reflected ray direction $\mathbf{r}$, with origin at $\mathbf{K}_\omega$, is

$$\mathbf{r} = \mathbf{S}_{m,\omega} - [(\mathbf{F} - \mathbf{K}_\omega)/|\mathbf{F} - \mathbf{K}_\omega|]/\lambda. \qquad (15)$$

This formula follows from the reflecting $\mathbf{S}_{m,\omega}$ being the bisector of the in and out rays $\mathbf{K}_\omega - \mathbf{F}$ and $\mathbf{r}$, respectively, and from $|\mathbf{S}_{m,\omega}| = 2\sin\theta_\lambda/\lambda$. The formula for the detector impact $\mathbf{R}$ in XYZ differs from that for the central impact, equation (9), because now the origin of $\mathbf{r}$ is not (0, 0, 0) but the final $\mathbf{K}_\omega$. This leads to

$$\mathbf{R} = \mathbf{K}_\omega + [(\mathbf{D} \cdot \mathbf{D} - \mathbf{K}_\omega \cdot \mathbf{D})/\mathbf{D} \cdot \mathbf{r}]\mathbf{r}. \qquad (16)$$

The detector coordinates (x_D, y_D) of $\mathbf{R}$ are found from equations (10); the particular impact occurs precisely at spindle rotation ω, equation (14).

Summarizing, each reflecting $(\mathbf{F}, \lambda, \mathbf{K}, \mathbf{S}_m)$ selection is mapped onto $X_D Y_D \omega$ real space as one impact (for $\zeta > 0$), with coordinates (x_D, y_D, ω). The three-dimensional mass of all possible (x_D, y_D, ω) impacts forms the reflection body; $\omega_{max} - \omega_{min}$ gives its ω lifetime. Note that the mapping is directed: the reverse path, from a particular impact (x_D, y_D, ω) to a unique $(\mathbf{F}, \lambda, \mathbf{K}, \mathbf{S}_m)$ combination, is not defined (precisely) and general impacts may coincide.

The central impact (§2.1) is in fact the general impact for the central values $(\mathbf{F}_0, \lambda_0, \mathbf{K}_0, \mathbf{S}_{m,0})$. Here $\mathbf{F}_0$ is the vector to the source centre, λ_0 is the central wavelength [$i.e.$ ($\lambda_{min} + \lambda_{max}$)/2], $\mathbf{K}_0$ is the 'vector' to the crystal element at (0, 0, 0), and $\mathbf{S}_0$ is the central mosaic vector (see Fig. 4). We use the central impact as a reference point for the general impacts; it does not necessarily lie in the midpoint of the reflection body.

3. The reflection boundary

The three-dimensional reflection boundary can be obtained as the smallest closed surface around 'all' general (x_D, y_D, ω) impacts, but this is not an efficient method: practically all impacts lie inside the body and provide no information about the external contour. We therefore select only the 'extreme' $(\mathbf{F}_E, \lambda_E, \mathbf{K}_E, \mathbf{S}_{m,E})$ combinations, among which are all general impacts ending on a reflection boundary vertex, as we will show in §3.2. In this formalism $\mathbf{F}_E$ is a vector to a vertex (extremum) of a rectangular strip, conforming to the actual focus dimensions, take-off angle and distance; that is, for a classic X-ray tube. Other kinds of sources ($e.g.$ a monochromator) should be simulated by a suitable convex polygon at an appropriate (possibly 'infinite') distance. λ_E corresponds to $\lambda_{\alpha 1}$ or $\lambda_{\alpha 2}$. (The line width is neglected: it amounts to only a few percent of the α_1–α_2 distance, but it could be included.) $\mathbf{K}_E$

is a vector to a relevant (idealized) crystal vertex, with the (convex) crystal in zero position. (A spherical crystal is represented by a regular dodecahedron in an arbitrary orientation, centred on the observed crystal centre.) $\mathbf{S}_{m,E}$ is one of the 16 evenly distributed vectors $\mathbf{S}_m$ on the (an)isotropic cone mantle (Fig. 4). (The number 16 is rather arbitrary, but adequate here.) In a typical example with four focus and eight crystal vertexes, we thus have $4 \times 2 \times 8 \times 16 = 1024$ $(\mathbf{F}_E, \lambda_E, \mathbf{K}_E, \mathbf{S}_{m,E})$ combinations, which, even so, give just as many impacts (x_D, y_D, ω). Even now only a minority of the impacts will lie on the reflection boundary, but at least we do not overlook reflection body vertexes, as follows from the 'contour adding method' described in §3.2. The desired three-dimensional hull around these 1024 impacts is a convex object with very many flat faces, of which most are triangles. It is rather cumbersome to construct and to examine whether a particular (x_D, y_D, ω) pixel belongs to it or not; therefore we will abandon this approach. The reasons we mentioned it at all are firstly that it describes the real problem, secondly that the actual $EVAL$-14 method is a simplification of it, and lastly, that we still do need $(\mathbf{F}_E, \lambda_E, \mathbf{K}_E, \mathbf{S}_{m,E})$-type impacts for other purposes.

We choose to represent the three-dimensional reflection boundary by three mutually perpendicular two-dimensional projections: $X_D Y_D$, $Y_D \omega$ and ωX_D, which are much easier to obtain and to apply.[3] The $X_D Y_D$ projection is familiar: it is the ω-integrated reflection spot on the detector; the others correspond to side views along X_D and Y_D, respectively. The last two projections are especially useful if the reflection and its surrounding background extend over more consecutive $\Delta\omega$ images, because then the background contribution is reduced compared with that of the $X_D Y_D$ projection alone. Pixels with at least one vertex within all three reflection projections are attributed to the peak region P; the remaining are attributed to the background region B.

We assemble two-dimensional $X_D Y_D$, $Y_D \omega$ and ωX_D reflection boundaries by convoluting calculated two-dimensional sub-reflection contours, as explained in §3.2, but first we give details of the individual sub-reflection calculations.
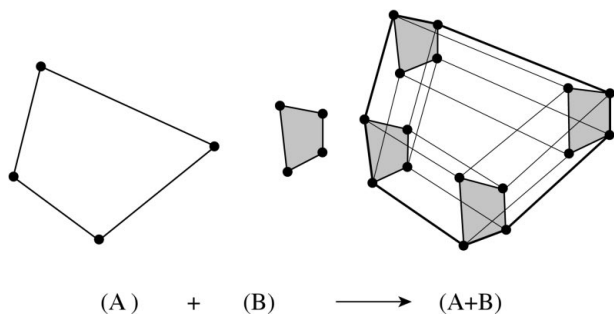
3.1. Sub-reflections

As mentioned already, a complete reflection can be thought of as the convolution of sub-reflections (Alexander & Smith, 1962). A sub-reflection is a hypothetical reflection resulting from only one of the factors focus, wavelength, crystal shape or mosaicity, while the remaining three factors are reduced to central ('point') values. For our reflection-contour predicting method, we need only the contours of the sub-reflections, not the intensity distribution within the contour. We describe the procedure for the $X_D Y_D$ contour; the $Y_D \omega$ and ωX_D contours are found in an analogous way.

---

[3] The three projections include of course a larger volume than the reflection body, but we accept this imperfection for the sake of the simplicity of the method.
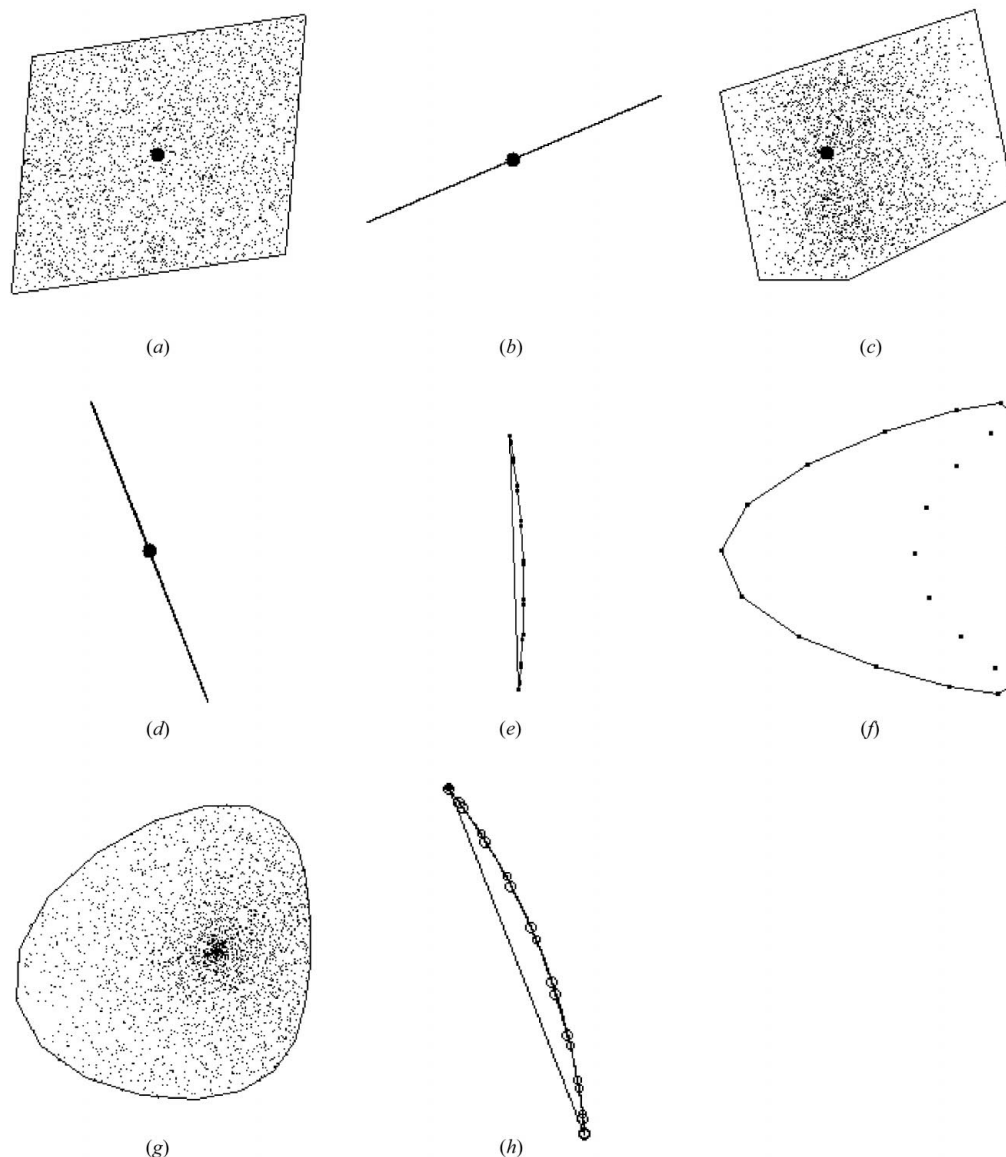
Figure 7
Various calculated sub-reflections, each with realistic values for one factor (*i.e.* for focus size, wavelength range, crystal size or crystal mosaicity), while the others are set to 'zero'. In (*e*) to (*h*) a surrealistic mosaic value is chosen, for instructive purposes. General data: detector distance 40 mm, swing-angle zero, $\theta = 20°$, $\chi = 20°$, except for (*e*) and (*f*), where $\chi = 2°$. Realistic values: focus (sealed tube) 0.3×3 mm, distance 220 mm, take-off angle 6.4°. λ range: 0.70930–0.71359 Å (Mo radiation). Crystal: three-sided skew prism with an overall size of $0.3 \times 0.4 \times 0.5$ mm. Mosaicity: 0.8°. (*a*) Focus $X_D Y_D$ sub-reflection. Closest surrounding box $x_D \times y_D$: 0.10×0.09 mm. 3000 arbitrary general impacts are shown; the large spot is the central impact. (*b*) λ $X_D Y_D$ sub-reflection; practically a straight line. Closest surrounding box $x_D \times y_D$: 0.28×0.12 mm. 3000 general impacts are shown, all lying on the line; the large dot is the central impact. (*c*) Crystal $X_D Y_D$ sub-reflection. Here the crystal is a skew three-sided prism with an overall size of $0.3 \times 0.4 \times 0.5$ mm. It is misscentred deliberately and therefore the central impact, from the crystal element $(0, 0, 0)$, does certainly not lie in the reflection centre. Closest surrounding box $x_D \times y_D$: 0.34×0.28 mm. The specks, from 3000 arbitrary impacts, show a greater density near the reflection centre, from the 'projection' of the crystal volume upon the detector. (*d*) Mosaic $X_D Y_D$ sub-reflection with 3000 mosaic impacts. Closest surrounding box $x_D \times y_D$: 0.18×0.47 mm. (*e*) Mosaic $X_D Y_D$ sub-reflection impacting near the X_D axis ($\chi = 2°$) for an unrealistic mosaicity of 15°. The 'powder arc' is clearly visible (x_D and y_D are on the same scale here). The dots on the arc are the impacts from 20 extreme mosaic vectors $\mathbf{S}_{m,E}$ (on the cone mantle, Fig. 4). By taking the convex hull (as we do) we include the surface between the string and the bow, but even here the practical effect for the complete reflection (Fig. 9*a*) is negligible. Closest surrounding box $x_D \times y_D$: 0.52×9.32 mm. (*f*) $X_D \omega$ sub-reflection for the same reflection as in (*e*); X_D runs horizontally in this figure. Here again the black dots are exact impacts from the same 20 extreme mosaic vectors as in (*e*). The convex hull here includes the region between the vertical line on the right (which runs along ω) and the skipped (seven) points. The practical effect is insignificant, as follows from the dimensions of the closest surrounding box $x_D \times \omega$: 0.52 mm × 15.0°. As follows from (*e*) and (*f*) the three-dimensional mosaic sub-reflection region forms a closed smooth convex domain on the 'powder cylinder'. The relevant part of this cylinder is obtained by translating (*e*) along ω, *i.e.* perpendicular to the plane of the figure, the detector. If the domain cuts the $X_D Y_D$ plane it overlaps itself in the Y_D projection, as in (*f*). (*g*) General mosaic XZ sub-reflection for a mosaicity of 30°. Closest surrounding box $x_D \times z_D$: 6.77 mm × 32.06°. If the mosaic sub-reflection lies completely above or below the detector $X_D Y_D$ plane (which is usually the case) the convex contour is correct; (*e*) and (*f*) show the exception. The sub-reflection is a deformed projection of the circular mosaic domain and therefore the central impact does not lie in the sub-reflection centre. The specks are from 3000 calculated arbitrary mosaic impacts. The greater density around the central impact results from an imposed Gaussian directional distribution model for the mosaic $\mathbf{S}_m$ vectors. (*h*) General mosaic XY sub-reflection for the same reflection as in (*g*). The small circles represent the impacts from the extreme mosaic vectors on the cone mantle. Closest surrounding box $x_D \times z_D$: 6.77 × 17.24 mm.

Figure 8
Adding the contours A and B by translating B along the edges of A. This method is applied repeatedly to construct a complete reflection from the calculated sub-reflections.

The source sub-reflection $X_D Y_D$ contour is the two-dimensional convex hull[4] (flat polygon) around the (x_D, y_D) coordinates of the special impacts $(\mathbf{F}_E, \lambda_0, \mathbf{K}_0, \mathbf{S}_0)$, *i.e.* those with $\mathbf{F}_E = \mathbf{F}_{E1}$, $\mathbf{F}_{E2}$, $\mathbf{F}_{E3}$ or $\mathbf{F}_{E4}$, respectively, if the focus has four vertexes, and central values λ_0, $\mathbf{K}_0$ and $\mathbf{S}_0$ for the other vectors.

The crystal sub-reflection $X_D Y_D$ contour is the convex hull around the (x_D, y_D) coordinates of the impacts $(\mathbf{F}_0, \lambda_0, \mathbf{K}_E, \mathbf{S}_0)$ for all relevant crystal vertexes $\mathbf{K}_E$.

The $X_D Y_D$ sub-reflection contour for the wavelength is the line from impact $(\mathbf{F}_0, \lambda_1, \mathbf{K}_0, \mathbf{S}_0)$ to impact $(\mathbf{F}_0, \lambda_2, \mathbf{K}_0, \mathbf{S}_0)$, and back: a contour is a closed loop.[5]

In the $X_D Y_D$ projection all 16 mosaic impacts $(\mathbf{F}_0, \lambda_0, \mathbf{K}_0, \mathbf{S}_{m,E})$ lie on a curved line through the central impact, which is actually a small part $(\mu/360)$ of the powder circle (with μ the full mosaic spread in degrees). [In fact, all mosaic impacts $(\mathbf{F}_0, \lambda_0, \mathbf{K}_0, \mathbf{S}_m)$ lie on this arc.] The corresponding convex hull looks like a bow with a string: all impacts lie on the bow; the empty string completes the contour. This unavoidably includes the surface between string and bow, but the practical consequences are negligible.

In the $Y_D \omega$ and ωX_D projections, the mosaic sub-reflection contours are more or less elliptical or egg-shaped loops. For reflections close to the detector X_D axis (*i.e.* $|\chi| \simeq 0$) they look partially folded up in the $Y_D \omega$ projection. For all practical purposes, however, the convex hull describes the sub-reflection shape adequately.

The $Y_D \omega$ and ωX_D contours for the crystal and source sub-reflections resemble their respective $X_D Y_D$ contours: a kind of skew shadow of the crystal and the focus. The $Y_D \omega$ and ωX_D wavelength contours are practically straight lines, as in the $X_D Y_D$ projection.

In Fig. 7 some calculated sub-reflection contours are shown, both for realistic and for strongly exaggerated parameter values.

---

[4] Methods to calculate the two-dimensional convex hull are described by Sedgewick (1984).
[5] Actually the λ sub-reflection is a very small part of a figure-of-eight-like curve centred on the through beam, as physically older crystallographers will remember from rotation diagrams.

3.2. Predicted two-dimensional reflection contours

The final two-dimensional contours are constructed by 'adding' the corresponding calculated contours of all sub-reflections. To add two contours A and B we translate B along the edges of A (Fig. 8). Note that we add only the contour shapes, not the contents. With more than two contours, as we have, we add the third to the sum $A + B$, *etc*. The adding sequence is immaterial: the operation is commutative. This contour convolution method supposes that the shape of contour B does not change significantly over the shift distances involved by moving it along the edges of A, *i.e.* the response function B applies to the whole A region. This is, by the way, also tacitly assumed in convolution formulae, such as presented by Alexander & Smith (1962) and thereafter. Not every extreme combination leads to a final contour vertex, but a vertex of this contour originates from some extreme combination indeed. For example, in Fig. 8 we have $4 \times 4 = 16$ extreme combinations (the black dots in $A + B$), but only 8 of these form the complete contour for $A + B$.

We can compare the predicted contour from the adding procedure with the real contour around 'all' impacts by firing random general impacts $(\mathbf{F}, \lambda, \mathbf{K}, \mathbf{S}_m)$ and seeing whether in the end the reflection contour is filled precisely, which is a fascinating phenomenon to watch on the computer screen. However, it is faster and more reliable to generate systematically the extreme impacts $(\mathbf{F}_E, \lambda_E, \mathbf{K}_E, \mathbf{S}_{m,E})$ only, because these constitute an infinitely small fraction of the general impacts and they surely include the final contour vertexes. Fig. 9 shows these impacts and the contours predicted by *EVAL*-14.

(a)   (b)
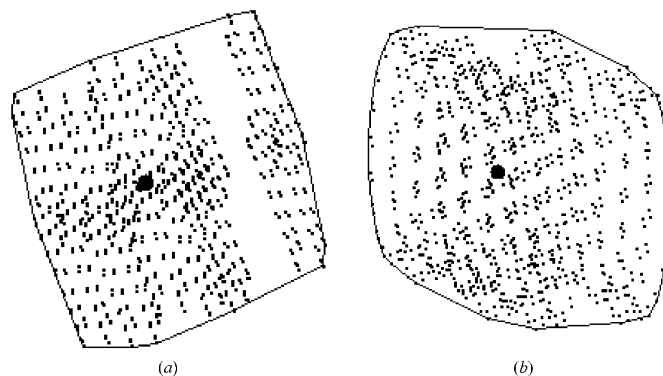
Figure 9
Predicted $X_D Y_D$ and $X_D Z \omega$ reflection contours, (a) and (b), respectively, obtained from the 'sum' (convolution) of the calculated sub-reflection contours for (F), (λ), (K) and (M) (*cf.* Figs. 7a–7d) by repeated application of the method illustrated in Fig. 8. The specks are the calculated 'extreme impacts', here $4 \times 2 \times 6 \times 20 = 960$ from the extreme combinations $(\mathbf{F}_E, \lambda_E, \mathbf{K}_E, \mathbf{S}_{m,E})$ from four focus, two λ, six crystal (three-sided skew prism) and 20 mosaic vertexes. [These 960 points correspond to the $4 \times 4 = 16$ dots for $(A + B)$ in Fig. 8.] The black dot is the central impact. The 'structure' arises from the extreme combinations not being random points. Somewhere in the left of the contour in (a) there is a convex part that should be concave, from the mosaic arc. This is clearly not visible. Reflection dimensions (closest surrounding box $x_D \times y_D \times \omega$): 1.15 mm $\times$ 1.65 mm $\times$ 1.63°. The size of this box may differ considerably per reflection (see Fig. 10). Parameters: detector distance 40 mm, swing $-30°$, focus 0.3 $\times$ 3 mm at 220 mm, take-off angle 5.7°, $\lambda_1 = 0.7093$, $\lambda_2 = 0.7136$ Å, crystal size 0.3 $\times$ 0.4 $\times$ 0.5 mm, mosaicity 1°.
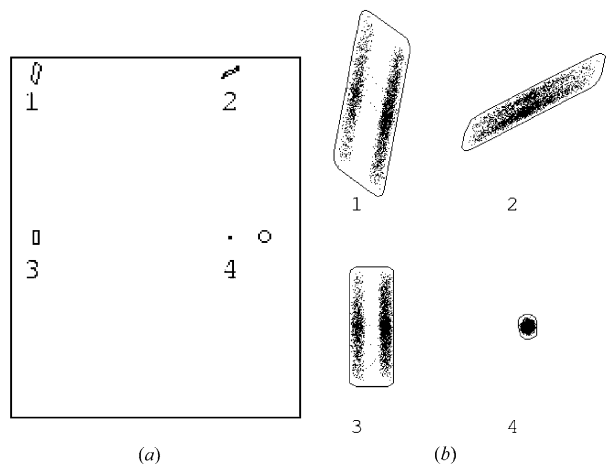
Figure 10
(*a*) Schematic representation of the whole detector with the predicted $X_D Y_D$ reflection contours for one and the same crystal but for different reflections, impacting at four indicated positions. 'o' is the primary beamstop. Parameters: focus 0.3×3 mm at 220 mm, take-off angle $5.7°$, $\lambda_1 = 0.7093$, $\lambda_2 = 0.7136$ Å, detector distance 40 mm, swing $= -35°$, spherical crystal diameter 0.2 mm, mosaicity $2°$. (*b*) The same reflections equally magnified. Note the α_1–α_2 splitting, especially in reflections 1 and 3. The specks within each contour are some calculated random impacts. Results: reflection size (closest surrounding box $x_D \times y_D \times \omega$): (1) 1.52 mm $\times$ 3.66 mm $\times$ $2.83°$ ($\theta = 37.19°$); (2) 2.84 mm $\times$ 1.92 mm $\times$ $13.60°$ ($\theta = 16.47°$); (3) 0.88 mm $\times$ 2.36 mm $\times$ $2.58°$ ($\theta = 35.94°$); (4) 3.10 mm $\times$ 0.35 mm $\times$ $2.14°$ ($\theta = 3.10°$). Reflection 2 (which would extend over 27 images if $\Delta\omega$ where $0.5°$, as in Fig. 11) is a typical example of a reflection that could well be rejected by *EVAL*-14 by the rule $|\chi| + \theta < 90° - \Delta$ (see §6).
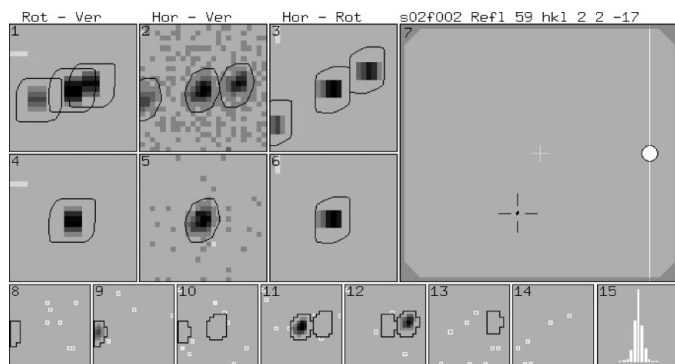
Figure 11
EVAL-14 at work on a twin lattice. Windows 8 through 14 show the primary data: seven slices each of 25×25 pixels with a $\Delta\omega$ depth of $0.5°$, forming the shoe box. The central contours in windows 10, 11 and 12 are the expected contours of the main reflection in those slices; the two (stronger) reflections extending over windows (8, 9, 10) left and (11, 12, 13) right are intruders from a twin lattice, falling neatly within their expected contours. Windows 1, 2 and 3 are the $y_D\omega$, $x_D y_D$ and ωx_D projections, respectively, of the complete shoe box. The row 4, 5 and 6 gives the final results: the aliens are eliminated and the *BPB* method can be applied successfully. Window 7 shows the complete detector with the position of the reflection under consideration (open black cross), detector centre (white cross) and primary beam impact (white circle); window 15 gives the net ω reflection profile. For details of the lattices see the work by Lutz *et al.* (1999).

3.3. Extra sub-reflection contours

We introduce extra sub-reflection contours to handle the mica effect and the detector point spread. The contours are simply added to the sum of the reflection contours so far, if applicable.

3.3.1. Satellite reflections from modulation. With modulated structures, *e.g.* mica-like substances, the reflection regions in reciprocal space are elongated symmetrically along a common direction **u**. Sometimes we can distinguish separate satellite reflections at regular distances from the main reflection $\mathbf{S}_0$; sometimes a more or less continuous streak of satellites is observed. In the first case the satellites can be evaluated separately; with streaks the complete region is evaluated as one reflection (leading to an averaged crystal structure). Then the projected sub-reflection contours (lines) run from the (x_D, y_D), (y_D, ω) or (ω, x_D) impact coordinates for $(\mathbf{F}_0, \lambda_0, \mathbf{K}_0, \mathbf{S}_0 - \mathbf{u}/2)$ to that for $(\mathbf{F}_0, \lambda_0, \mathbf{K}_0, \mathbf{S}_0 + \mathbf{u}/2)$ and back, with $|\mathbf{u}|$ the length of the satellite region. Note that θ_λ varies along **u** as $\sin\theta_\lambda = \lambda|\mathbf{S}_0 + c\mathbf{u}|/2$, with c varying from $-\frac{1}{2}$ to $+\frac{1}{2}$.

3.3.2. Detector point spread. The point-spread effect refers to the phenomenon that (strong) radiation hitting one pixel may affect neighbouring pixels. We simulate a circular effective point-spread contour on the detector by a suitably sized regular polygon centred on the central impact. We do not have to calculate impacts here: the edges of the polygon itself directly form the extra sub-reflection contour.

4. Net intensities and weights

Our intensity evaluation method is essentially a *BPB* method. Shoe-box pixels with at least one vertex inside the three calculated contours are considered as gross peak data (N_P pixels); the others are considered as background (N_B pixels), typically 200 and 1500, respectively. A linear least-squares local background function $B(x_D, y_D)$ is calculated through the N_B background pixels:

$$B(x_D, y_D) = ax_D + by_D + c. \tag{17}$$

Background pixels deviating more than $3\sigma(B)$ per pixel [see equation (20)] are excluded and a new least-squares background is calculated, in an iterative process.

The net intensity per pixel in the P region, $I_{\text{net,pp}}$, is obtained by subtracting the final $B(x_D, y_D)$:

$$I_{\text{net,pp}}(x_D, y_D, \omega) = P(x_D, y_D, \omega) - B(x_D, y_D). \tag{18}$$

If, for a not too weak reflection, the centre of gravity of the reflection body from all $I_{\text{net,pp}}$ pixels differs significantly from the expected centre, the predicted (x_D, y_D), (y_D, ω) and (ω, x_D) reflection contours are shifted accordingly and the whole peak/background discriminating process is repeated. By this, some pixels will be renamed from peak to background pixel, and *vice versa*. If there is no reason to shift anymore an extra final shift corresponding to the difference between the central impact for $\lambda = (2\alpha_1 + \alpha_2)/3$ and for $\lambda = (\alpha_1 + \alpha_2)/2$ is applied. This allows, in a first approximation, for the difference between the centre of gravity and the middle of the net reflection region. Especially for higher θ angles, as occur in small-molecule work, the last shift is not negligible at all.

Finally, the net intensity for the complete reflection, I_{net}, is found by adding $I_{net,pp}(x_D, y_D, \omega)$ from equation (18) for all N_P pixels in the final P region:

$$I_{net} = \sum_{N_P} I_{net,pp}(x_D, y_D, \omega). \qquad (19)$$

In general the pixel values $P(x_D, y_D, \omega)$ are not on an absolute scale, but the relation between these values and Poissonian X-ray counts is rather well known: one Poissonian X-ray count increments a pixel value by about 1.6; the exact value depends on the actual detector. We therefore can apply the simple *a priori* Poisson sigma, $\sigma(N) = N^{1/2}$, if we divide all observations by '1.6'. Then [strictly speaking only for a centred centro-symmetrically shaped reflection, or for a and b physically zero in equation (17)] $\sigma(I_{net}) = (P + k^2 B)^{1/2}$, with $P = \sum_{N_P} P(x_D, y_D, \omega)$, $k = N_P/N_B$ and $B = \sum_{N_B} B(x_D, y_D, \omega)$, *i.e.* the sum over all observed B pixels, not the calculated B values from (17).

We propose a quality factor Q, a kind of peak/background ratio, which can very well serve as a relative weight. For Q we do not need to know the factor '1.6' and there are no restrictions imposed upon a or b in (17) or upon the reflection shape or position. First we calculate sigma per pixel for the background by pixelwise comparison of the observed intensities $B_{obs}(x_D, y_D, \omega)$ with the calculated background $B(x_D, y_D)$ from (17):

$$\sigma(B) = \left[(N_B - 3)^{-1} \sum_{N_B} \left| B_{obs}(x_D, y_D, \omega) - B(x_D, y_D) \right|^2 \right]^{1/2}. \qquad (20)$$

This gives a quite reliable estimation by the large number of independent background data N_B. Sigma expected for the total background extending under the N_P peak pixels is $\sigma(B) N_P^{1/2}$; hence we define the quality factor Q as

$$Q = I_{net} / \left[\sigma(B) N_P^{1/2} \right]. \qquad (21)$$

Note that Q is entirely based on observed pixel intensities. It appears that reflections with $Q < 10$ (roughly) are too weak to be observed on our KappaCCD.

If the background within a shoe box depends significantly on ω this must be included in equation (17) as $B(x_D, y_D, \omega) = ax_D + by_D + c\omega + d$. Then in (19) and (20) $B(x_D, y_D)$ becomes $B(x_D, y_D, \omega)$, and in (20) $(N_B - 3)$ will read $(N_B - 4)$. This may occur with long-living reflections, extending over many $\Delta\omega$ images (which, by the way, should be discarded, as is discussed in §6).

5. Alien reflections

When the diffraction pattern originates from two lattices we find both lattices with the indexing program *DIRAX* (Duisenberg, 1992).[6] We denote the main lattice and its reflections by *A* and the secondary by *B*. Both reciprocal cell and orientation matrixes $[\mathbf{R}_A]$ and $[\mathbf{R}_B]$ are supplied to

EVAL-14, which calculates the expected contours for the main reflection *A* and those for *B* reflections not lying completely outside the *A* shoe box. Interfering neighbours *A′* from *A* itself, as can happen with very short reciprocal axes, are also treated as aliens. If in a $\Delta\omega$ image the reflection region *B* is completely separated from *A*, all pixels in that layer belonging to *B* are ignored both for peak and back-ground calculations. If *B* and *A* overlap partially, the intensity in the region *A* + *B* is distributed over *A* and *B* in the ratio *A/B* obtained from non-overlapping regions, in an iterative process. If the reflections overlap almost completely the sum is output.

When lattice *A* has been evaluated we usually reverse roles for *A* and *B* and evaluate all images for the *B* reflections. Fig. 11 illustrates twin-lattice handling.

6. Comments and discussion

In *EVAL*-14 a purely kinematical reflection process is assumed, *i.e.* an $(\mathbf{F}, \lambda, \mathbf{K}, \mathbf{S}_m)$ combination results in one reflected ray with a precise reflection angle $2\theta_\lambda$ given by Bragg's Law. This model is not always applicable, *e.g.* not with fibres, where an appreciable $\Delta 2\theta$ range may arise from the mosaic blocks consisting of very few cells and where cell dimensions may vary somewhat through the crystal. At the moment there are no provisions for this lattice distortion in the public KappaCCD version of *EVAL*-14, but it is a subject of investigation at our laboratory.

Reflections with not a single $(\mathbf{F}, \lambda, \mathbf{K}, \mathbf{S}_m)$ combination yielding $\cos\zeta \leq 1$ [equation (11)] are completely absent in all images: the 'cusp reflections'. For reflections with $\cos\zeta \simeq 1$ for the central impact [*i.e.* $|\chi| + \theta \simeq 90°$, equation (4)] there are two possibilities. First, some combinations do reflect (those with $\cos\zeta \leq 1$), but others never will ($\cos\zeta > 1$), no matter how long we rotate ω; then we have an essentially incomplete reflection. Note that this is not the same as a partial reflection, which continues in the adjacent $\Delta\omega$ image. Secondly, $\cos\zeta \leq 1$ (but still $\cos\zeta \simeq 1$) for all $(\mathbf{F}, \lambda, \mathbf{K}, \mathbf{S}_m)$ combinations. This may seem to be a complete normal reflection, but we reject it nevertheless. Reflections with $\cos\zeta \to 1$ extend over many $\Delta\omega$ images, as follows directly from the calculated ω size of the reflection body. In classic terms, such reflections are slowly grazing the Ewald sphere instead of quickly traversing it. Moreover, the Lorentz part of the Lp factor is unreliable and the absorption coefficient can vary considerably during the long reflection lifetime. Finally, these reflections may be self-overlapping, that is if in a $\Delta\omega$ image the (x_D, y_D) impact regions for the $+\zeta$ and $-\zeta$ positions cross the line of inter-section of the XZ plane with the detector. (For a perpendicular detector this line is the Y_D axis in Fig. 1.) To avoid all this we require $|\chi| + \theta < 90° - \Delta$, with Δ amply allowing for mosaicity, focal and crystal angular width, and the wavelength range effect, *e.g.* $\Delta = 6°$. If the excluded and cusp reflections are absolutely needed and no equivalent reflections are available, then one or two extra data collection runs are

---

[6] If there are more than two lattices involved *DIRAX* will find these too, but then expert *à la carte EVAL*-14 data handling comes into play.

necessary with the crystal in suitably different orientations.[7] On a single-axis diffractometer this requires crystal re-mounting in appropriate orientations.

The general impact equation (11) is also applicable to an experiment with the spindle making an oblique angle with the X axis, the primary beam. We only have to express all relevant vectors in an auxiliary system $X'Y'Z'$ with Z' along that rotation axis and, for convenience, with X' in $\mathbf{F}_0Z'$. It should be noted that this is a less favourable experimental setup, for at least two reasons. In the first place, fewer reflections will be activated during a full spindle rotation. For example, in the extreme situation that the spindle coincides with the primary beam, not one reflection will be integrated. Only relatively few accidentally activated, incomplete reflections will circulate on the detector, thereby forming powder rings. Secondly, for all reflections the ω lifetime increases (with consequences mentioned in the paragraph immediately above), as follows directly from the calculated $\omega_{max} - \omega_{min}$ range [equation (14)]. In the same degenerate example, spindle along X, the few active, incomplete reflections last forever and no others will ever come to life.

The anisotropy vector $\mathbf{A}$ is easily found with a four-circle diffractometer [from ψ scans (Duisenberg, 1983)], but with an area detector some experimenting and educated-guesswork is needed. Mosaic anisotropy manifests itself by unexpected variations in reflection size; more specifically, by a larger 'powder arc' on the detector and/or a longer ω lifetime than predicted by the isotropic $\mathbf{S}_m$ model. Reflections with $\mathbf{S}_0$ perpendicular to $\mathbf{A}$ are affected most and this may give a clue: $\mathbf{A}$ runs along $\mathbf{S}_0^{(1)} \times \mathbf{S}_0^{(2)}$, if $\mathbf{S}_0^{(1)}$ and $\mathbf{S}_0^{(2)}$ are two such reflections. Moreover, $\mathbf{A}$ is directed usually along a simple direct- or reciprocal-lattice vector.

Effective values for source size and distance can best be established occasionally by experiments with a small perfectly centred high-quality test crystal, aided by the EVAL-14 (graphical) output; this is an instructive activity.

We do not exploit three-dimensional reflection profiles in EVAL-14 yet, but these can be constructed from a set of suitably sampled and weighted general impacts, corrected for absorption. Such an a priori profile might be interesting for a predicted-profile fitting method (PPF) and therefore it is a subject under active investigation in our laboratory.

The general impact model is also suited to describe von Laue reflections. In a Laue experiment the crystal remains fixed in the same ω position for all reflections. The reflection condition for an arbitrary $(\mathbf{F}, \mathbf{K}, \mathbf{S}_m)$ combination can be fulfilled only by presenting an X-ray with wavelength λ_m corresponding to θ_m from the actual angle $90° - \theta_m$ between $\mathbf{F}$ – $\mathbf{K}$ (along the primary beam) and $\mathbf{S}_m$. This wavelength is $\lambda_m = 2\sin\theta_m/|\mathbf{S}_m|$ (and harmonics) and each combination will reflect its own λ_m from the source, if available. We can calculate the reflection contour (and neighbour overlap) on the detector, but also the total active λ range. If, as a consequence of a very asymmetrical crystal shape or mis-centring, the λ ranges for a

pair of Bijvoet reflections differ in such a way that only one range includes a significant absorption edge, an (extra) intensity anomaly may arise. Laue reflection handling is not implemented yet in the EVAL-14 procedure.

7. Conclusion

EVAL-14 is a robust intensity evaluation method. Reflections are integrated by the BPB principle, where the reflection boundary P is predicted from a few physical constants and experimental parameters. The method can cope with notoriously problematic situations, such as a far from spherical crystal, anisotropic mosaicity, α_1–α_2 peak splitting, interference from close neighbours, twin lattices or satellite reflections, streaks from modulated structures, and heavy absorption effects upon the profile, where other integration methods might fail.

The 'general impact' formulation allows future prediction of (complicated) reflection profiles.

For information on the EVAL-14 program, contact a.m.m.schreurs@chem.uu.nl.

References

Alexander, L. E. & Smith, G. S. (1962). Acta Cryst. **15**, 983–1004.
Bolotovsky, R., White, M. A., Darovsky, A. & Coppens, P. H. (1995). J. Appl. Cryst. **28**, 86–95.
Bourgeois, D., Nurizzo, D., Kahn, R. & Cambillau, C. (1998). J. Appl. Cryst. **31**, 22–35.
Diamond, R. (1969). Acta Cryst. A**25**, 43–55.
Duisenberg, A. J. M. (1983). Acta Cryst. A**39**, 211–216.
Duisenberg, A. J. M. (1992). J. Appl. Cryst. **25**, 92–96.
Ford, G. C. (1974). J. Appl. Cryst. **7**, 555–664.
Graafsma, H., Svensson, S. O. & Kvick, Å. (1997). J. Appl. Cryst. **30**, 957–962.
Kabsch, W. (1988). J. Appl. Cryst. **21**, 916–924.
Keulen, E. (1969). Doctoral thesis, Groningen University. (In Dutch, with a summary in English.)
Lehmann, M. S. & Larsen, F. K. (1979). Acta Cryst. A**30**, 580–584.
Leslie, A. G. W. (1991). Molecular Data Processing, in Crystallographic Computing 5, edited by D. Moras, A. D. Podjarny & J. C. Thierry. Oxford University Press.
Lutz, M., Hagen, H., Schreurs, A. M. M., Spek, A. L. & Van Koten, G. (1999). Acta Cryst. C**55**, 1636–1639.
Mathieson, A. McL. & Stevenson, A. W. (1996). Crystallogr. Rev. **6**, 59–155.
Otwinowski, Z. (1993). Proceedings of the CCP4 Study Weekend, compiled by L. Sawyer, N. Isaac & S. Bailey, pp. 56–62. Warrington: Science and Engineering Research Council/Daresbury Laboratory.
Otwinowski, Z. & Minor, W. (1997). Processing of X-ray Diffraction Data Collected in Oscillation Mode, in Methods in Enzymology, Vol. 276. New York: Academic Press.
Pflugrath, J. W. & Messerschmidt, A. (1993). MADNES Reference Manual, v. 2.4, Nonius Delft BV, Delft, The Netherlands.
Rossmann, M. G. (1979). J. Appl. Cryst. **12**, 225–238.
Sedgewick, R. (1984). Algorithms. Reading: Addison-Wesley.

---

[7] The 'Hursthouse rotations'. Private communication from M. B. Hursthouse to AJMD, London, 1990.